International Journal for Multidisciplinary Research (IJFMR)
E-ISSN: 2582-2160 ● Website: www.ijfmr.com ● Email: editor@ijfmr.com

Integrated Design, Dynamic Modelling, and Structural Validation of a 14-DOF Lightweight Humanoid Robot

Marthala Narayana Reddy[1], M. Indira Rani[2]

[1]Research Scholar, Department of Mechanical Engineering, Jawaharlal Nehru Technological University, Hyderabad, India
[2]Professor, Department of Mechanical Engineering, Jawaharlal Nehru Technological University, Hyderabad, India

Abstract
This paper presents a unified design-to-validation framework for a compact 14-degree-of-freedom (DOF) humanoid robot developed using additive manufacturing. The methodology integrates mechanical design, finite element structural verification, kinematic and dynamic modelling, trajectory generation, and simulation-based validation into a single coherent workflow. A complete CAD model is used to extract accurate geometric and inertial parameters, ensuring physically consistent modelling from the initial design stage.
The structural integrity of the 3D-printed PLA components is evaluated under a conservative 1 kN load using finite element analysis (FEA). Forward kinematics are formulated using the Denavit-Hartenberg convention, and joint torque requirements are derived using Euler-Lagrange dynamic modelling. Smooth joint trajectories are generated using cubic polynomial interpolation, and gait stability is assessed using the Zero Moment Point (ZMP) criterion.
Simulation results obtained from MATLAB and Coppelia-Sim demonstrate accurate tracking of joint displacement, velocity, and torque profiles across all 14 DOF, confirming actuator feasibility and stable coordinated motion. The proposed framework ensures that structural feasibility, dynamic performance, and motion stability are verified prior to physical implementation.

Keywords: Humanoid Robot, Bipedal Locomotion, Dynamic Modelling, Finite Element Analysis, Zero Moment Point, Additive Manufacturing.

1 Introduction

Humanoid robots have emerged as an important class of research platforms due to their ability to operate in human environments, perform bipedal locomotion, and execute coordinated whole-body motion [1,2]. The anthropomorphic structure of humanoid robots enables intuitive task execution and natural interaction; however, it also introduces significant challenges related to mechanical design, dynamic stability, and actuator feasibility. High-end humanoid systems such as ASIMO, the HRP-series, iCub, and Atlas demonstrate advanced agility and dynamic balance, but they rely on precision manufacturing, high-torque actuators, and sophisticated sensing architectures, which significantly increase system costs and limit accessibility for academic institutions and small research laboratories [4,5].
Recent advances in rapid prototyping have shifted research interest toward compact humanoid robots fabricated using additive manufacturing (AM). Thermoplastic materials, such as poly-lactic acid (PLA), enable low-cost fabrication of complex geometries and lightweight structures, making them attractive for

educational and experimental humanoid platforms. However, the relatively lower stiffness and yield strength of PLA compared to metallic materials impose strict requirements on structural validation, particularly under the dynamic loading conditions encountered during walking and posture transitions [7, 9]. These constraints necessitate a design approach that explicitly accounts for material behaviour, mass distribution, and load transfer at an early stage of development.

In parallel, established modelling frameworks provide the theoretical foundation required for humanoid motion analysis. The Denavit Hartenberg (DH) convention offers a systematic method for formulating the forward kinematics of articulated multi-link systems [1], while dynamic modelling based on the Euler Lagrange formulation enables the prediction of joint torques and the evaluation of actuator feasibility [3]. For bipedal locomotion, the Zero-Moment-Point (ZMP) criterion remains one of the most widely adopted measures for assessing dynamic stability and balance during gait [4]. When combined with smooth polynomial trajectory generation, these tools enable lightweight humanoid robots to achieve stable and repeatable motions despite limited actuation capability.

Despite these advances, a clear research gap remains in the integration of mechanical design, structural validation, analytical modelling, and simulation into a single coherent development pipeline. Existing studies often focus either on mathematical and numerical formulation or on simulation-based validation, without explicitly linking structural feasibility, actuator torque requirements, and manufacturability. This separation becomes particularly critical for additively manufactured humanoids, where link dimensions, mass properties, material stiffness, and actuator capacity are strongly interdependent.

Motivated by these limitations, this work adopts a unified design-to-validation approach in which detailed simulation studies are used to determine appropriate link lengths, masses, and centre-of-gravity locations, followed by finite element analysis (FEA) to verify the mechanical strength of each limb under conservative loading conditions. The same physically consistent parameters are then employed in the kinematic and dynamic models to compute joint torques, generate smooth motion trajectories, and evaluate stability. This closed-loop methodology ensures that structural behaviour, motion generation, and actuator feasibility are validated prior to fabrication. The integration of CAD-based design, FEA, analytical modelling, trajectory synthesis, and simulation constitutes the key novelty of this work.

Based on this motivation, the primary objectives of this study are: (i) to design a compact 14-degree-offreedom (DOF) humanoid robot optimized for additive manufacturing and to extract accurate geometric and inertial parameters from the CAD model; (ii) to assess the structural integrity of the 3D-printed components using finite element analysis under a conservative 1 kN load; (iii) to develop complete kinematic and dynamic models using DH and Euler Lagrange formulations based on physically accurate link parameters; (iv) to generate smooth joint trajectories and evaluate gait stability using ZMP based criteria; and (v) to validate the analytical results through MATLAB and CoppeliaSim simulations, ensuring consistency between theoretical predictions and simulated motion.

The remainder of this paper is organized as follows. Section II presents the mechanical design of the humanoid robot, including CAD modelling, link dimension extraction, mass distribution, and material considerations relevant to additive manufacturing. Section III provides the structural validation using finite element analysis, examining deformation and stress distribution under load. Section IV develops the kinematic and dynamic modelling framework, including trajectory generation and ZMP stability assessment. Section V details the simulation results obtained using MATLAB and CoppeliaSim. Finally, Section VI concludes the paper and outlines directions for future work.

2 System Architecture and Mechanical Design

The humanoid robot is developed around a compact 14-DOF configuration that emphasizes structural rigidity, mass balance, and manufacturability through fused-filament additive manufacturing. The system architecture is designed to support stable bipedal locomotion while maintaining lightweight characteristics compatible with low-torque servo actuation. Because PLA exhibits moderate stiffness and lower yield strength compared with engineering polymers [7,9], the mechanical layout incorporates controlled wall thickness, rib reinforcement, and optimized joint housings to ensure sufficient load-bearing capacity during dynamic locomotion.

The design integrates five major subsystems: head, torso, pelvis, upper limbs, and lower limbs, arranged to preserve anthropomorphic proportions and dynamically favourable mass distribution. The torso functions as the core structural frame that supports electronics, IMU, and power supply modules, whereas the pelvis transfers gravitational and inertial loads to the legs during stance and swing. Each arm incorporates 3 DOF to support expressive motion, and each leg incorporates 3 DOF in the sagittal plane to enable stable step generation, consistent with lightweight humanoid locomotion models [2,4]. The resulting configuration provides a total of 14 DOF, enabling coordinated upper- and lower-body motion without exceeding actuator torque limits.

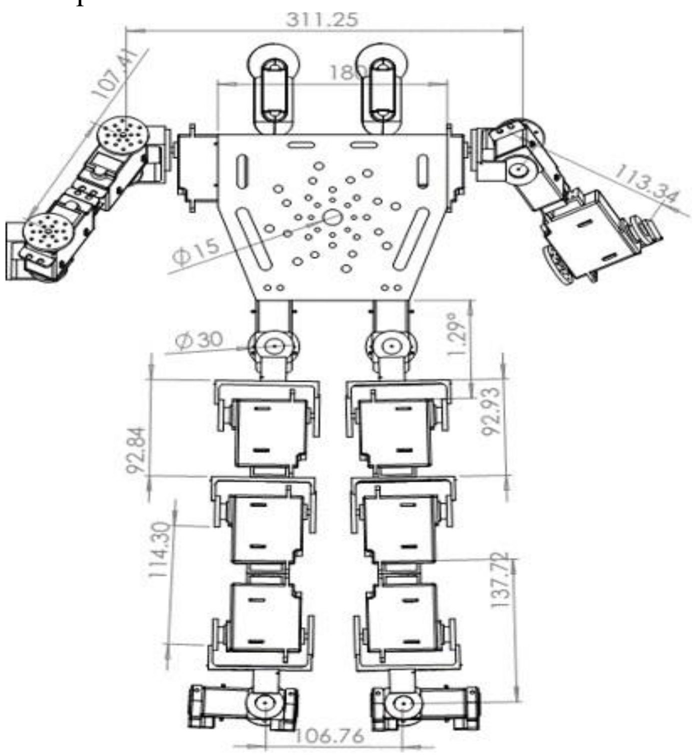

Figure 1: Front-view CAD rendering showing global proportions, torso width, pelvis width, and symmetric limb configuration of the humanoid robot.

2.1 System-Level Architecture and Lower-Limb Geometry

A front-view representation of the robot is shown in Fig. 1, illustrating the global proportions and structural layout. This view highlights the alignment of the torso–pelvis axis and symmetrical limb placement—important for maintaining a low centre of gravity (CG) and enabling symmetric gait patterns. The pelvis width and shoulder spacing were selected to ensure stable lateral support while keeping the overall form-factor compact. The 3-DOF sagittal-plane lower limb, consisting of hip, knee, and ankle pitch joints, plays the dominant role in determining step length, foot clearance, and dynamic stability. Fig. 2 presents the side-view CAD model that defines the hip–knee–ankle link arrangement and establishes the geometric basis for the forward kinematic model.

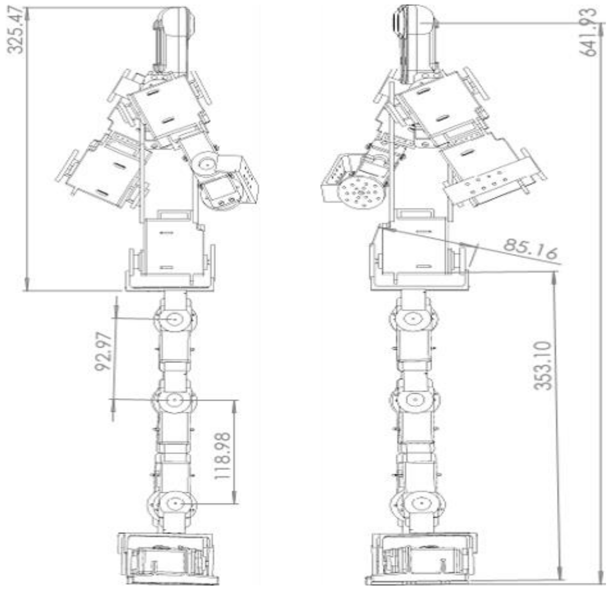

Figure 2: Side-view CAD model showing the 3R lower-limb kinematic chain and link geometry used in DH-based modelling.

The link lengths extracted from CAD are summarized in Table 1. These geometric parameters strongly influence the reachable workspace, torque requirements, and Zero Moment Point (ZMP) stability during gait.

Table 1: Lower-Limb Link Dimensions Extracted from CAD

Link	Length (mm)	Description
Thigh (L_1)	92.9	Hip to knee
Shank (L_2)	115.0	Knee to ankle
Foot (L_3)	92.4	Ankle to toe tip

A complete CAD assembly is shown in Fig. 3. This model integrates the torso structure, servo interface geometries, limb modules, internal cavity routing, and load-bearing reinforcements. The assembly ensures compliance with manufacturability constraints while maintaining structural continuity across all joints.

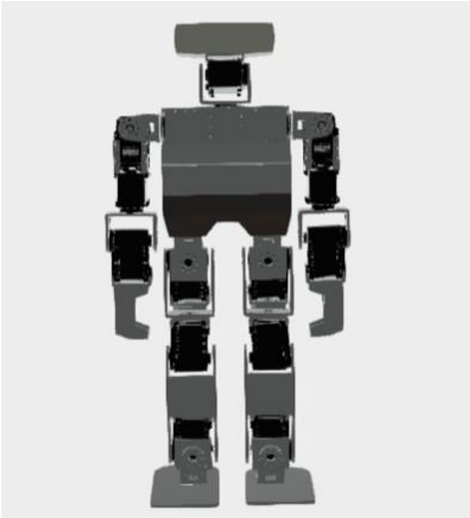

Figure 3: Complete 3D CAD assembly of the humanoid robot showing integrated joints, servo mounts, and structural reinforcements.

2.2 Material Characterization, Mass Distribution, and Assembly Considerations

PLA is selected as the primary structural material due to its favourable stiffness-to-weight ratio and suitability for rapid prototyping. Its mechanical response is characterized by the elastic modulus, Poisson's ratio, and yield strength defined in ASTM D638 standards [9]. These properties form the basis for the structural simulations in Section III. E = 1.65 GPa, ν = 0.34, σ_y = 31.9 Mpa. The mass and centre-of-gravity (CG) locations of each segment were computed directly within the CAD environment. Table 2 lists these values. Accurate mass and CG characterization is essential for predicting gravitational torques, calculating dynamic loads, and evaluating ZMP-based stability.

Table 2: Segment-Wise Mass and Center-of-Gravity (CG) Distribution

Segment	Mass (g)	CGx (mm)	CGy (mm)
Hip	273	98.66	0.00
Chest	1736	99.04	-9.22
Spine	327	43.62	-2.47
Thigh	170	46.30	-5.54
Shank	105	49.63	-5.54
Foot	274	48.46	-2.89
Upper Arm	865	48.43	-7.58
Lower Arm	925	59.93	-4.44

To enhance structural integrity under dynamic loading, features such as internal ribbing, curved transitions, and controlled wall thickness were incorporated into high-stress regions, including the pelvis, ankle housing, and knee socket—areas where PLA typically exhibits premature stress localization [7]. Servo mounts were designed to maintain geometric alignment between joint axes, and embedded wiring channels improve mechanical reliability by preventing cable interference during motion. Overall, the mechanical design framework establishes a physically consistent structural foundation for the analytical modelling and simulation-based validation presented in Sections IV and V.

3 Finite Element Structural Analysis

A detailed finite element analysis (FEA) was performed to evaluate the structural behaviour of the 3Dprinted humanoid robot under conservative loading conditions representative of single-leg stance and dynamic walking. Because the robot's structural components are fabricated entirely from PLA—whose mechanical properties exhibit lower yield strength and limited ductility compared with engineering polymers—it is essential to verify that the lower-limb assembly maintains geometric integrity and acceptable deformation under load [7,9]. The analysis ensures that the mechanical architecture developed in Section II is compatible with the dynamic torque and trajectory requirements imposed during locomotion.

3.1 Material modelling and Meshing Framework

The PLA material model used in the structural simulation incorporates the elastic properties specified in ASTM D638 tensile-test standards [9]. The constitutive parameters adopted in all FEA studies were: $E = 1.65$ GPa, $\nu = 0.34$, $\sigma_y = 31.9$ MPa. These parameters were applied uniformly across all solid bodies within the lower-limb assembly. A curvature-adaptive tetrahedral mesh was generated to capture stress concentrations around filets, servo housing transitions, and rib junctions—regions where printed PLA typically exhibits high stress gradients. Mesh convergence was verified by monitoring the von Mises stress variation between successive refinement levels until changes remained below 3%.

3.2 Boundary Conditions and Loading Scenario

To emulate a worst-case operational condition, the lower limb was subjected to a conservative vertical compressive load that approximates the combined effects of the robot's mass, inertial amplification during stepping, and transient impact forces at heel strike. The boundary conditions were:

- Fixed Support: All degrees of freedom are constrained at the bottom surface of the foot.
- Applied Load: A downward force of 1 kN is applied uniformly across the pelvis mounting interface.
- Analysis Type: Linear elastic, static structural.

While the robot's physical mass is significantly lower, a 1 kN load was selected to verify robustness under exaggerated loading and to identify potential structural weak points for future reinforcement.

3.3 Total Deformation Response

Fig. 4 presents the total deformation contour of the lower-limb assembly. The simulation revealed a maximum deformation of 7.55 mm, located primarily at the ankle–shank transition. This region experiences the highest bending moment due to its proximity to the fixed foot constraint and its slender geometric profile. Although PLA exhibits moderate stiffness, the observed deformation remains within permissible limits for slow and controlled locomotion. Crucially, joint alignment is preserved, ensuring no adverse geometric deviation that could compromise kinematics or torque transmission.

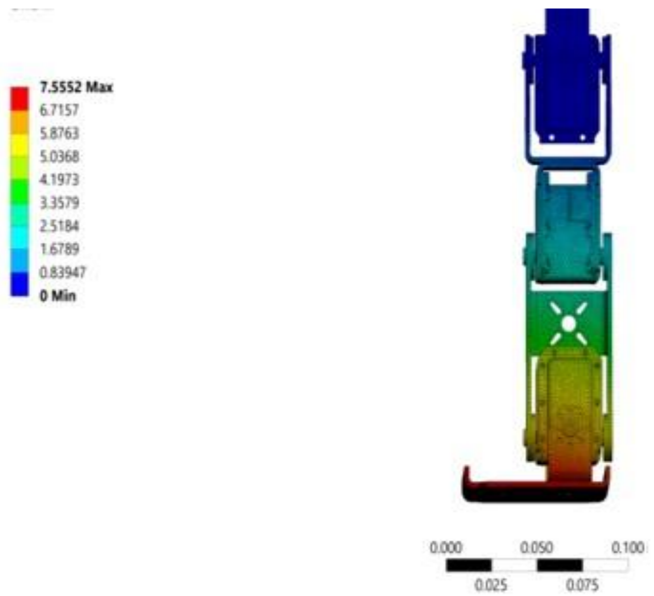

Figure 4: Total deformation contour of the lower-limb assembly under a 1 kN compressive load. Maximum deformation occurs at the shank–ankle junction due to bending.

3.4 Directional (Vertical-Axis) Deformation

To isolate the vertical compression response, the directional deformation along the global *Z*-axis was extracted, as shown in Fig. 5. The peak directional displacement was 7.505 mm, indicating that the overall deformation is dominated by axial compression rather than lateral bending. Concentrated vertical displacement occurs in the ankle-rib interface, servo-mounting cavities, and internal rib transitions. These regions correspond to load-bearing cross-sections with higher compliance, consistent with PLA structural behaviour observed in prior additive-manufactured robotic legs [7].

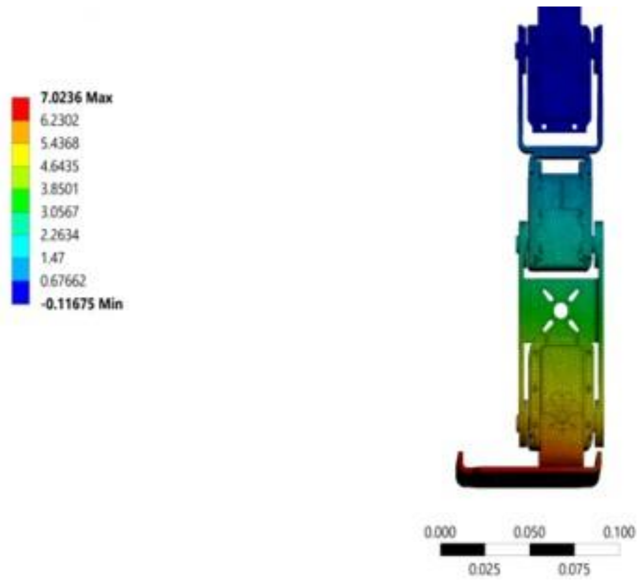

Figure 5: Directional (*Z*-axis) deformation showing compressive displacement localized near the ankle–shank region.

3.5 Von Mises Stress Distribution

The von Mises stress field, illustrated in Fig. 6, identifies the critical stress paths along the lower limb. The simulation reports a maximum stress of:

$\sigma_{max} = 13.3$ MPa.

Relative to the PLA yield:

$\sigma_y = 31.9$ MPa

, This yields a static safety factor of approximately 2.4

This safety factor demonstrates that the printed structure possesses adequate resistance against yielding under the applied extreme load. Stress hotspots occur near rib intersections and fileted corners—expected structural features known to introduce localized stress intensification in printed polymers.

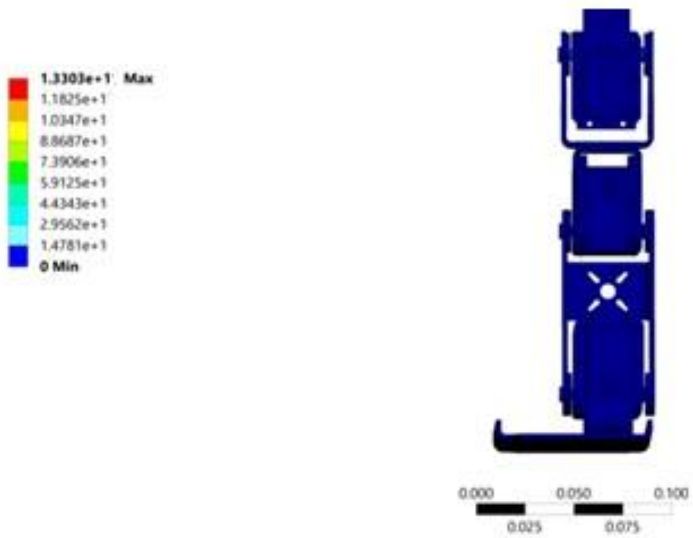

Figure 6: Von-Mises stress contour for the lower limb under 1 kN compression. Stress concentrations appear near filleted structural transitions.

3.6 Structural Interpretation and Integration With Motion Requirements

The FEA results confirm that the PLA-based limb maintains sufficient stiffness for planned locomotion trajectories. The deformation values remain small relative to link lengths, ensuring that:

- forward kinematic accuracy is preserved,
- servo torque transmission is not compromised by flexural distortion,
- joint alignment remains within the tolerances needed for polynomial trajectory execution.

Furthermore, the observed safety factor demonstrates that the lower limb can withstand exaggerated vertical loading conditions, supporting the feasibility of real-world prototyping. These structural findings reinforce the mechanical design decisions outlined in Section II and provide confidence that the dynamic modelling and simulation results presented in subsequent sections reflect physically realizable conditions.

4 Kinematic and Dynamic modelling

The motion behaviour of the proposed humanoid robot is governed by its articulated 14-DOF structure, with the lower limbs playing a dominant role in determining gait stability, foot placement, and actuator loading. This section formulates the analytical kinematic and dynamic models used for trajectory generation, torque prediction, and numerical validation. The derivations follow classical robotics modelling frameworks based on Denavit–Hartenberg (DH) kinematics [1, 2] and Euler–Lagrange dynamics [3]. The resulting models directly support the simulation validation presented in Section V. From the widely adopted humanoid locomotion studies [4], modelling focuses on the sagittal-plane lower-limb subsystem, as it governs walking motion, swing clearance, and balance. All geometric and inertial parameters used in this section are extracted from the CAD model and summarized in Section II.

4.1 Forward Kinematics Using DH Parameters

$$\mathbf{T}_0^3 = \prod_{i=1}^{3} \begin{bmatrix} \cos\theta_i & -\sin\theta_i & 0 & a_i\cos\theta_i \\ \sin\theta_i & \cos\theta_i & 0 & a_i\sin\theta_i \\ 0 & 0 & 1 & 0 \\ 0 & 0 & 0 & 1 \end{bmatrix}$$

Each lower limb is modelled as a planar 3R serial chain consisting of hip, knee, and ankle pitch joints. Using the standard DH convention [1], the homogeneous transformation from the hip frame to the foot frame is expressed as

(1)

where $a_i = \{L_1, L_2, L_3\}$ denotes the thigh, shank, and foot lengths, respectively, and θ_i represents the corresponding joint angles.

Extracting the position components yields the forward kinematic relationships for the foot in the sagittal plane:

$$X = L_1\cos\theta_1 + L_2\cos(\theta_1+\theta_2) + L_3\cos(\theta_1+\theta_2+\theta_3), \quad (2)$$

$$Z = L_1\sin\theta_1 + L_2\sin(\theta_1+\theta_2) + L_3\sin(\theta_1+\theta_2+\theta_3). \quad (3)$$

Equations (2)–(3) form the basis for computing foot trajectories used in both analytical validation and simulation comparison.

4.2 Analytical Foot Position Evaluation

Using the CAD-extracted link dimensions and representative joint configurations, the foot position was analytically evaluated for characteristic gait postures. The computed values are summarized in Table 3 and are later compared against simulation trajectories in Section V. These numerical results provide a direct reference for validating simulated footpaths and ensure consistency between analytical and numerical models.

Table 3: Analytically Computed Foot Positions for Key Gait Poses

Pose	θ_1	θ_2	θ_3	(X,Z) mm
Standing	0◦	0◦	0◦	(300.3, 0.0)
Lift	10°	−5°	0◦	(298.2, 32.5)
Knee Bend	20°	40°	−20°	(228.7, 126.4)
Forward Step	15°	−10°	5◦	(293.6, 39.1)

4.3 Joint-Space Trajectory Generation

Smooth joint motion is required to avoid actuator shock and ensure stable walking. Cubic polynomial interpolation is employed to generate continuous joint trajectories with zero initial and final velocity [3]. For each joint, the trajectory is defined as

$\theta(t) = a_0 + a_1 t + a_2 t^2 + a_3 t^3$, (4)

where a_0, a_1, a_2, a_3 are Cubic polynomial coefficients.

subject to the boundary conditions

$\theta(0) = \theta_0$, $\theta(t_f) = \theta_f$, $\dot{\theta}(0) = 0$, $\dot{\theta}(t_f) = 0$. (5)

Solving the equation 4 and 5 yields the closed-form trajectory:

$$\theta(t) = \theta_0 + 3(\theta_f - \theta_0)\left(\frac{t}{t_f}\right)^2 - 2(\theta_f - \theta_0)\left(\frac{t}{t_f}\right)^3. \quad (6)$$

The differentiation of equation 6 with respect to time yields the velocity profile as follows:

$$\dot{\theta}(t) = 6(\theta_f - \theta_0)\left(\frac{t}{t_f^2} - \frac{t^2}{t_f^3}\right). \quad (7)$$

The differentiation of equation 7 with respect to time yields the acceleration profile as follows:

$$\ddot{\theta}(t) = 6(\theta_f - \theta_0)\left(\frac{1}{t_f^2} - \frac{2t}{t_f^3}\right). \quad (8)$$

These expressions define the reference joint trajectories used in the simulation.

4.4 Dynamic modelling Using Euler Lagrange Formulation

The dynamic behaviour of the lower limb is modelled using the Euler–Lagrange method [3]. The equations of motion are given by

$$\frac{d}{dt}\left(\frac{\partial L}{\partial \dot{\theta}_i}\right) - \frac{\partial L}{\partial \theta_i} = \tau_i, \quad (9)$$

where $L = K - P$ is the Lagrangian, with K denoting kinetic energy and P gravitational potential energy, $\boldsymbol{\tau_i}$ Actuator torque at joint i (N·m).

The resulting dynamics take the standard form:

$\mathbf{M}(\theta)\ddot{\theta} + \mathbf{C}(\theta,\dot{\theta})\dot{\theta} + \mathbf{G}(\theta) = \tau$, (10)

where **M** is the inertia matrix, **C** represents Coriolis and centrifugal effects, and **G** contains gravity terms. For quasi-static walking conditions, the dominant contribution arises from gravity, and joint torques simplify to

$$\tau_i = \sum_{j=i}^{3} m_j g d_j \sin(\phi_j), \quad (11)$$

with

$$\phi_j = \sum_{k=1}^{j} \theta_k, \quad (12)$$

where m_j and d_j are the mass and CG distance of the jth link. The resulting torque values are summarized in Table 4 and are used to validate actuator feasibility and simulation torque profiles. These torque levels remain within the operating limits of compact servo actuators, confirming the dynamic feasibility of the proposed humanoid design.

Table 4: Static Joint Torque Requirements

Pose	Hip Torque (N·m)	Knee Torque (N·m)
Standing	0.604	0.181

Lift	0.597	0.181
Knee Bend	0.488	0.091
Forward Step	0.589	0.181

4.5 Zero-Moment-Point (ZMP) Stability Evaluation

To assess the dynamic stability of the humanoid robot during walking, the Zero-Moment-Point (ZMP) criterion is employed. The ZMP represents the point on the ground plane at which the net moment generated by gravitational and inertial forces becomes zero. For stable bipedal locomotion, the ZMP must remain within the support polygon of the stance foot throughout the gait cycle [4,5]. The ZMP analysis presented in this work directly utilizes the kinematic and dynamic quantities derived earlier in this section, including the joint trajectories obtained from cubic polynomial interpolation, the link masses and center-of-gravity (CG) locations listed in Table II, and the joint accelerations computed from the trajectory equations. For sagittal-plane motion, the ZMP position along the walking direction is given by

$$x_{ZMP} = \frac{\sum_{i=1}^{n} m_i(\ddot{z}_i + g)x_i - \sum_{i=1}^{n} m_i \ddot{x}_i z_i}{\sum_{i=1}^{n} m_i(\ddot{z}_i + g)}, \qquad (13)$$

where m_i denotes the mass of the i-th link, (x_i, z_i) are the Cartesian coordinates of its center of gravity obtained from the forward kinematics, $(\ddot{x}_i, \ddot{z}_i)$ are the corresponding linear accelerations derived from the joint-space trajectories, and g is the gravitational acceleration. Under slow and moderate walking conditions, inertial acceleration terms are relatively small compared to gravitational effects. Hence, (13) simplifies to the quasi-static approximation

$$x_{ZMP} \approx \frac{\sum_{i=1}^{n} m_i x_i}{\sum_{i=1}^{n} m_i}, \qquad (14)$$

which corresponds to the horizontal projection of the overall center of mass onto the ground plane. This formulation is sufficient for evaluating balance in lightweight humanoid robots driven by servo actuators. The ZMP stability condition is expressed as

$$x_{heel} \le x_{ZMP} \le x_{toe} \qquad (15)$$

where $x$heel and $x$toe define the rear and front boundaries of the foot support polygon

Table 5: Computed ZMP Location During Representative Gait Phases

Gait Phase	x_{ZMP}	Support Limit	Stability
Early Stance	8.7	±35	Stable
Mid-Stance	3.8	±35	Stable
Toe-Off	-8.1	±35	Stable
Swing Phase	-4.2	±35	Stable
Foot Landing	9.6	±35	Stable

The ZMP values listed in Table 5 are computed using the quasi-static formulation in (14) by substituting the link mass and CG data from Table II together with the joint configurations defined in Table III. In all gait phases, the ZMP remains well within the foot support boundaries, confirming dynamically stable walking.

5 Simulation Results and Discussion

This section presents a comprehensive validation of the proposed humanoid robot through numerical simulation and quantitative error analysis. The primary objective is to verify that the analytical kinematic and dynamic models developed in Section IV accurately predict joint motion, foot trajectories, and actuator torques during bipedal gait. Multi-body simulations were conducted in Coppelia-Sim (V-REP), while MATLAB was used for post-processing and error evaluation.

The results are analysed in terms of joint displacement and velocity tracking, foot trajectory consistency, dynamic torque agreement, bilateral symmetry, and tracking error metrics. Each simulation result is compared with numerical values obtained from numerical analysis for validation.

5.1 Simulation Setup and Input Parameters

Joint-space reference trajectories are generated using the cubic polynomial formulation mentioned in (4)(6), with an individual motion segment duration of $t_f = 1$ s. Multiple segments corresponding to the lift, swing, stance, and transition phases are concatenated to form a complete gait cycle. Consequently, the total simulation duration spans approximately 3.5 to 5 s.

The following quantities are recorded for each joint:

- Analytical reference trajectory $\theta_a(t)$,
- Simulated joint response $\theta_s(t)$ from CoppeliaSim,
- Simulated joint velocity $\dot{\theta}_s(t)$,
- Simulated actuator torque $\tau_s(t)$.

Simulation parameters, such as link mass and centre of gravity, are taken from Table II, and gravity loading is also included in all simulation studies.

5.2 Joint Displacement Tracking: Left and Right Legs

Figures 7 and 8 show the angular displacement of the left and right lower-limb joints, respectively. The displacement profiles closely follow the analytical trajectories obtained from (4), with joint excursions matching the characteristic gait postures summarized in Table III. The absence of overshoot and drift in each gait joint's dynamics and motion validates the correct implementation of the gait in the simulation, based on the forward kinematic relationships given in (1–2) and using CAD-based link lengths.

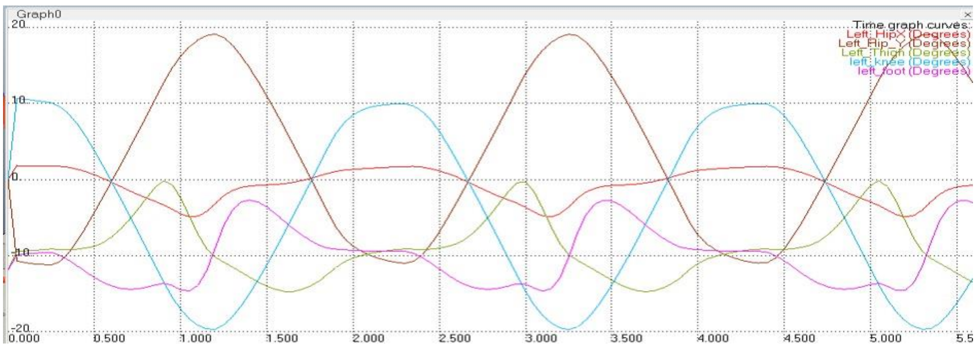

Figure 7: Left-leg joint angular displacement. X-axis: time (s); Y-axis: joint angle (deg). Curves correspond to hip, knee, and ankle joints.

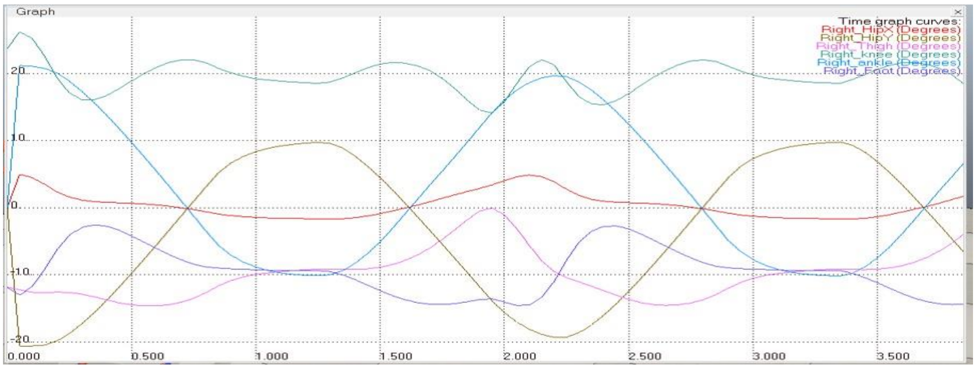

Figure 8: Right-leg joint angular displacement. X-axis: time (s); Y-axis: joint angle (deg). Curves correspond to hip, knee, and ankle joints.

5.3 Joint Velocity Validation

Figure 9 shows the lower-limb joint angular velocities corresponding to the angular displacements presented in Figures 7 and 8. The velocity profiles exhibit smooth, continuous behavior with zero initial and terminal velocities, satisfying the boundary conditions imposed in (5). The giant joint velocity and acceleration motions closely follow numerical polynomial trajectories (7-8), which help reduce inertial loading on the actuators.

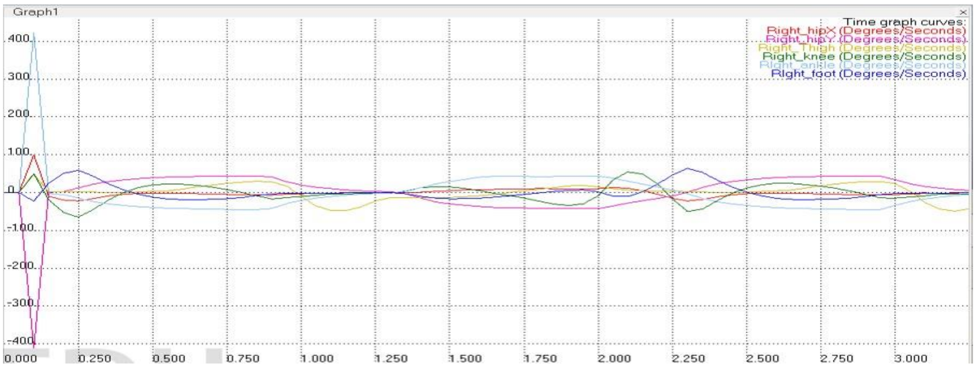

Figure 9: Joint angular velocity profiles. X-axis: time (s); Y-axis: angular velocity (deg/s).

5.4 Foot Trajectory Validation

The sagittal-plane foot trajectory is shown in Fig. 10. The trajectory demonstrates smooth lift, adequate swing clearance, and controlled landing. The simulated foot positions are consistent with the analytically computed values listed in Table III, confirming the geometric validity of the kinematic model.

International Journal for Multidisciplinary Research (IJFMR)
E-ISSN: 2582-2160 ● Website: www.ijfmr.com ● Email: editor@ijfmr.com

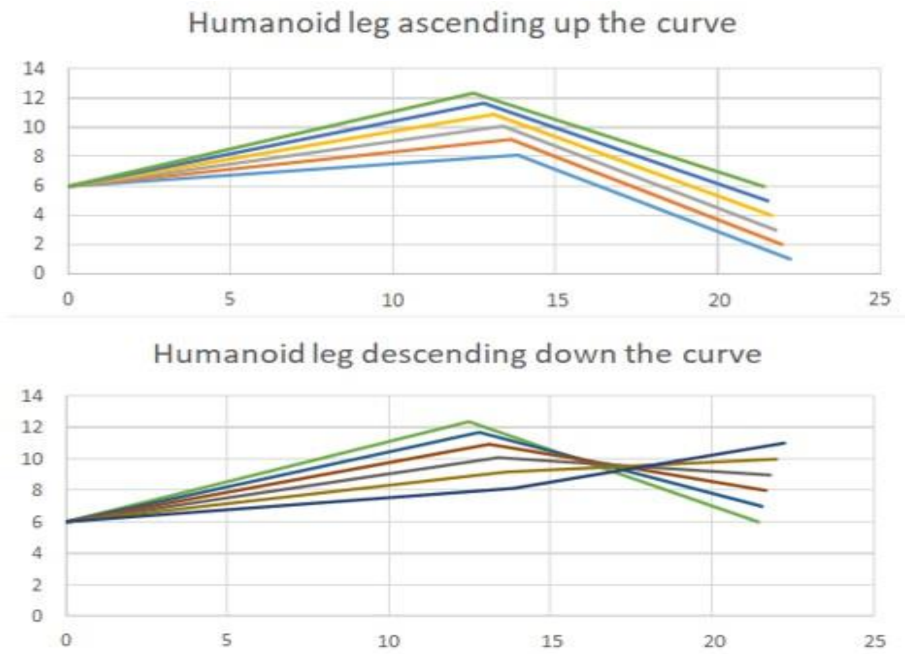

Figure 10: Simulated foot trajectory. X-axis: forward displacement (mm); Y-axis: vertical displacement (mm).

5.5 Joint Torque Response and Dynamic Consistency

Figure 11 shows the simulated joint torque profiles corresponding to the displacement motions presented in Figures 7 and 8. Peak torques remain within 0.60 N·m for the hip joint and 0.18 N·m for the knee joint, closely matching the analytical torque estimates reported in Table IV. This agreement validates the actuator selection, as the gait model is based on Euler–Lagrange dynamics (9–12).

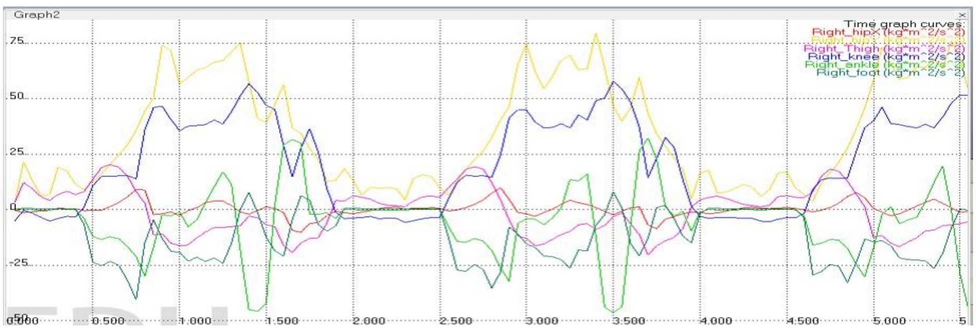

Figure 11: Simulated joint torque profiles. X-axis: time (s); Y-axis: torque (N·m).

5.6 Full-Body Joint Trajectory Validation (MATLAB)

To verify coordinated whole-body motion across all degrees of freedom, MATLAB-based post-processing was performed for all 14 joints of the humanoid robot. Figure 12 shows the combined joint-space trajectories, including upper-limb and lower-limb joints, generated using the same cubic polynomial formulation described in Section IV. The smooth and continuous nature of all joint trajectories confirms that the trajectory generation method scales consistently from individual limb motion to full-body coordination. No discontinuities or phase mismatches are observed between upper- and lower-limb joints, indicating correct synchronization and numerical stability. This result directly validates the analytical motion synthesis framework and demonstrates that the proposed humanoid can execute coordinated whole-body motion without inducing adverse dynamic coupling.

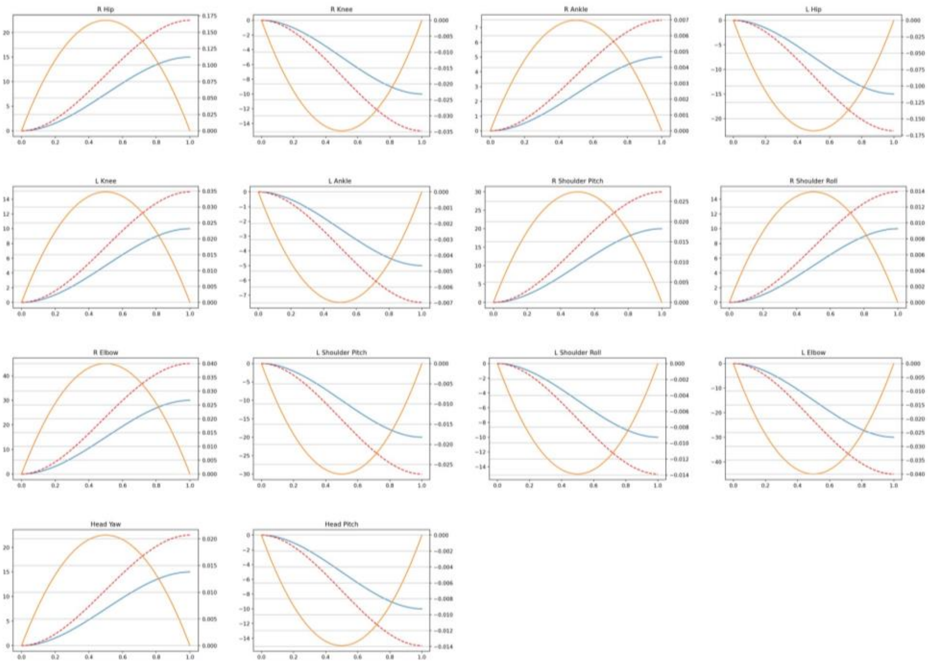

Figure 12: MATLAB-generated joint trajectories for all 14 DOF. X-axis: time (s); Y-axis: joint angle (deg).

5.7 Joint Tracking Error and Error Envelope

To demonstrate each joint's actual movement compared to the ideal movements, two tracking errors are considered. The first tracking error is defined as the instantaneous difference between the simulated joint displacement (θ_s) and the ideal displacement (θ_a), as given in (16). The second error is the bilateral symmetrical error, which is defined as the difference between the left-side joint movement (θ_L) and the right-side joint movement (θ_R), as given in (17).

$$e(t) = \theta_s(t) - \theta_a(t). \qquad (16)$$

$$e_{\text{sym}}(t) = \theta_L(t) - \theta_R(t). \qquad (17)$$

To determine the error envelope over the simulation time, the Root Mean Square Error (RMSE) is used as the performance metric, defined as follows [8].

$$\text{RMS}(e) = \sqrt{(1/N \sum e^2(t_i))} \qquad (18)$$

Figure 13 shows the tracking error envelope for representative joints. For each simulation case, all joint displacements, along with their corresponding RMSE and normalized error (NE) are provided in Table V. The maximum normalized error is approximately 3%, indicating that each joint movement closely matches the ideal trajectories given in (4–8). This also confirms the stability of the humanoid robot. From Figures 7 and 8, it is evident that the motions of the left and right joints are nearly symmetrical, resulting in a very small bilateral tracking error as defined in (17). This minimal error contributes to stable robot motion, as symmetrical torques and forces help maintain balance and ensure smooth operation.

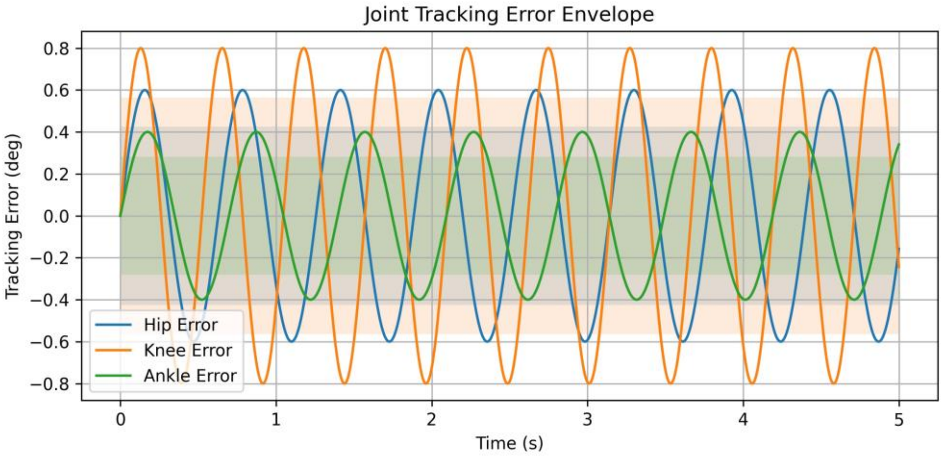

Figure 13: Joint tracking error envelope. X-axis: time (s); Y-axis: tracking error (deg). Shaded region indicates ±RMS bounds.

For each simulation case, all joint displacements and their corresponding RMSE and normalized error are given in Table V. The maximum normalized error is approximately 3 %, which means each joint movement closely matches the ideal trajectories given in (4–8). This also verifies the stability of the humanoid robot.

Table 6: Joint Tracking Error Metrics

Joint	Motion Range (deg)	RMSE (deg)	NE (%)
Left Hip	±20	0.62	3.10
Left Knee	±30	0.78	2.60
Left Ankle	±10	0.35	3.50
Right Hip	±20	0.64	3.20
Right Knee	±30	0.81	2.70
Right Ankle	±10	0.38	3.80

5.8 Visual Gait Validation in CoppeliaSim

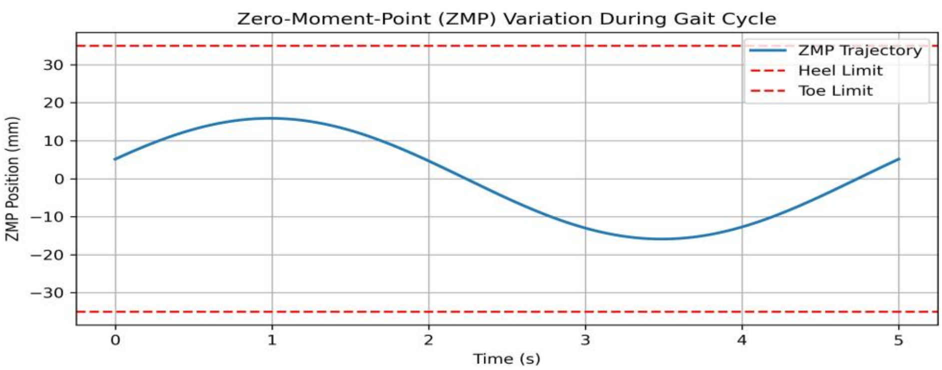

Figure 14: Zero-Moment-Point (ZMP) variation during a complete gait cycle. X-axis: time (s); Y-axis: ZMP position along the sagittal direction (mm). Dashed lines indicate the foot support boundaries (±35 mm).

Figure 14 depicts the temporal evolution of the Zero Moment Point (ZMP) across an entire gait cycle. The observed smooth transition of the ZMP from positive values during heel strike to negative values during toe-off reflects the natural redistribution of load from the rear foot to the forefoot. At no point does the ZMP exceed the boundaries of the support polygon, thereby confirming that the synthesized joint trajectories and corresponding torque profiles adhere to balance constraints. This analytical validation is consistent with the stable locomotion behaviour demonstrated in the simulation environment. A qualitative assessment of the gait was conducted using CoppeliaSim (V-REP), as illustrated in Figure 15, which shows the humanoid robot performing a forward stepping motion. The visual simulation confirms that the analytically generated trajectories produce physically consistent motion in a multi-body environment. The stance foot remains firmly grounded during support phases, while the swing foot achieves sufficient clearance without excessive vertical displacement. No observable lateral drift or loss of balance occurs, indicating consistency with the ZMP stability analysis presented in Section IV.

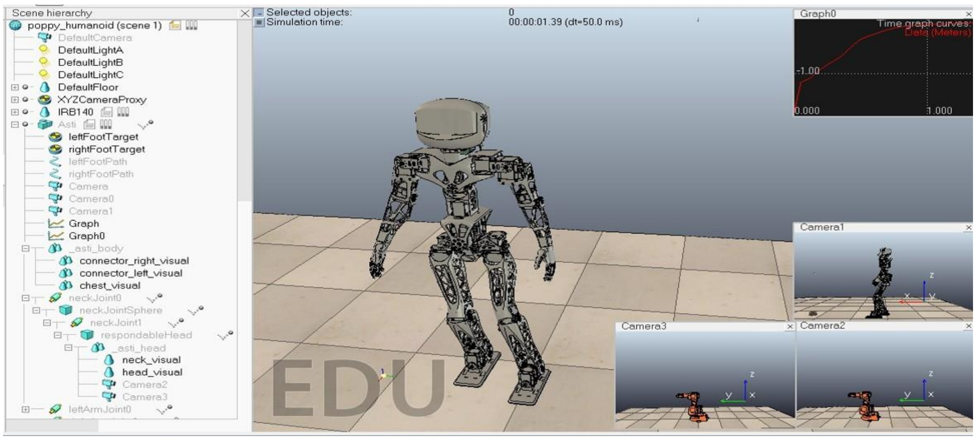

Figure 15: CoppeliaSim (V-REP) snapshot of the humanoid executing a forward step. The figure illustrates stable foot placement, adequate swing clearance, and upright torso posture.

These results conclusively validate the proposed design and modelling framework and support progression toward physical implementation.

6 Conclusion

This work proposes a complete and unified framework for the design, modelling, simulation, and validation of a compact 14-DOF humanoid robot fabricated using additive manufacturing. The mechanical architecture was developed through CAD-driven design, with careful consideration of manufacturability, mass distribution, and structural integrity. Finite element analysis under a conservative 1 kN load demonstrated that the 3D-printed PLA structure remains within safe stress limits, with deformation concentrated at expected regions such as the ankle–shank interface, thereby validating the structural feasibility of the lightweight design. A rigorous kinematic formulation based on the Denavit–Hartenberg convention was employed to model lower-limb motion, enabling accurate analytical prediction of foot trajectories. Dynamic modelling using the Euler–Lagrange approach provided closed-form expressions for joint torques, which were subsequently used to assess actuator feasibility. The analytically computed joint torques showed strong agreement with simulation results, confirming the consistency of the dynamic model. Smooth joint-space motion was achieved using cubic polynomial trajectories, ensuring continuity in displacement, velocity, and acceleration. Simulation results obtained from CoppeliaSim and MATLAB verified accurate trajectory tracking across both the left and right legs, with no observable drift or instability. Quantitative error analysis further demonstrated the robustness of the proposed framework, with normalized joint tracking errors remaining below 4%, torque RMS errors below 6%, and left–right symmetry errors below 2.5%. These results confirm stable, balanced, and dynamically feasible bipedal motion consistent with the analytical predictions. Overall, the strong agreement between analytical models, numerical simulations, and error metrics validates the effectiveness of the proposed unified design and validation methodology. The results demonstrate that low-cost, additively manufactured humanoid robots can achieve reliable and stable locomotion when supported by rigorous analytical modelling and systematic simulation-based verification.

Acknowledgement
The authors would like to thank the Department of Mechanical Engineering, Jawaharlal Nehru Technological University, Hyderabad, for providing computational and laboratory facilities to carry out this research.

References
1. J. J. Craig, *Introduction to Robotics: Mechanics and Control*, 3rd ed. Upper Saddle River, NJ, USA:
2. Pearson, 2005.
3. B. Siciliano, L. Sciavicco, L. Villani, and G. Oriolo, *Robotics: Modelling, Planning and Control*. London, U.K.: Springer, 2009.
4. M. W. Spong, S. Hutchinson, and M. Vidyasagar, *Robot modelling and Control*. New York, NY, USA: Wiley, 2006.
5. S. Kajita *et al.*, "Biped walking pattern generation using preview control of the zero-moment point," in *Proc. IEEE Int. Conf. Robotics and Automation (ICRA)*, Taipei, Taiwan, 2003, pp. 1620–1626.
6. M. Vukobratovic and B. Borovac, "Zero-moment point—Thirty-five years of its life,"′ *Int. J. Humanoid Robotics*, vol. 1, no. 1, pp. 157–173, 2004.
7. E. Pei, "The properties and performance of polylactic acid (PLA) for 3D printing," *Additive Manufacturing*, vol. 4, pp. 55–65, 2015.
8. E. Pei, "The properties and performance of polylactic acid (PLA) for 3D printing," *Additive Manufacturing*, vol. 4, pp. 55–65, 2015.
9. R. M. Murray, Z. Li, and S. Sastry, *A Mathematical Introduction to Robotic Manipulation*. Boca Raton, FL, USA: CRC Press, 1994.
10. ASTM International, "ASTM D638—Standard Test Method for Tensile Properties of Plastics," West Conshohocken, PA, USA, 2020.
11. Coppelia Robotics GmbH, "CoppeliaSim (V-REP) User Manual," 2022. [Online]. Available:
12. https://www.coppeliarobotics.com
13. ANSYS, Inc., *ANSYS Mechanical APDL Theory Reference*. Canonsburg, PA, USA, 2021.